

Freestanding Cellulose Acetate/ZnO Flowers Composites for Solar Photocatalysis and Controlled Zinc Ions Release

Giuseppe Arrabito,^{a,*} Giuseppe Prestopino,^b Pier Gianni Medaglia,^b Vittorio Ferrara,^a Giuseppe Sancataldo,^a Giuseppe Cavallaro,^a Francesco Di Franco,^c Michelangelo Scopelliti,^{a,d,e} Bruno Pignataro^{a,d}

^a Department of Physics and Chemistry - Emilio Segrè, University of Palermo, Viale delle Scienze, Ed. 17, 90128 Palermo, Italy

^b Department of Industrial Engineering, University of Rome “Tor Vergata”, Via del Politecnico 1, 00133 Rome, Italy

^c Department of Engineering, University of Palermo, Viale delle Scienze, Ed. 6, 90128 Palermo, Italy

^d National Interuniversity Consortium of Materials Science and Technology (INSTM), UdR of Palermo, 50121 Florence, Italy

^e ATeN Center, University of Palermo, Viale delle Scienze 18/A, 90128 Palermo, Italy

*Corresponding author. E-mail address: giuseppedomenico.arrabito@unipa.it

Abstract

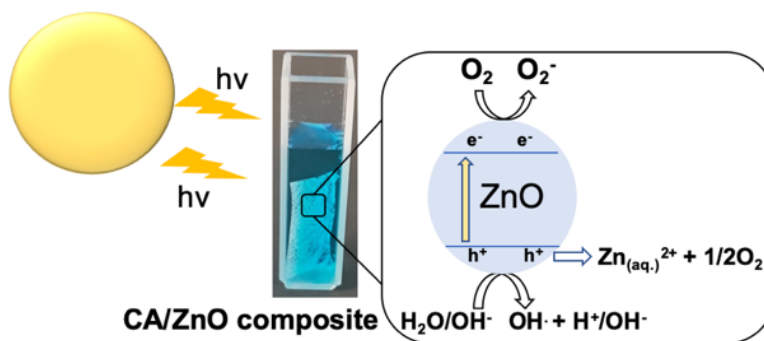
ZnO based materials have received wide interest in bioremediation and medicine, given their biocompatibility, photocatalytic and antibacterial properties. However, the application of bare self-supported ZnO is potentially hampered by their dissolving behavior, which could be controlled by producing out-of-equilibrium composites with biocompatible polymeric systems to reduce their direct exposure to the fluid in which they are dispersed. Herein, this work explores tailored ZnO

flowers/cellulose acetate (CA) photocatalytic composites at different ZnO weight percentages (1-15 wt%). The morphological and physico-chemical properties of the composites are investigated by SEM, XPS, XRD, UV-Vis, thermogravimetry and contact angle measurements. The photocatalytic degradation of methylene blue dye under simulated solar light is studied, finding an optimal value of ZnO filler loading in the polymer. Electrochemical impedance spectroscopy allows to accurately monitor the release of ionic species under dark conditions, observing a direct proportionality to the ZnO-loading in the polymer, as a result of its degradation in aqueous environments.

KEYWORDS. ZnO nanostructures, photocatalysis, cellulose films, electrochemical sensors, electrochemical impedance spectroscopy.

KEYWORDS. ZnO nanostructures, photocatalysis, cellulose films, electrochemical impedance spectroscopy.

Graphical Abstract



1. Introduction

The design of sustainable, biocompatible and highly efficient water decontamination approaches has a preeminent importance in the public health management. In fact, the necessity of clean water

supplies is not always worldwide guaranteed, especially in third world countries, as it is hampered by the industrial wastes [1], microplastics pollution [2] and antibiotics leakages in the aquatic environment [3]. A solution to these threats could be heterogenous photocatalysis, an approach that uses sustainable almost unlimited source of energy – *i.e.* Sun – to produce degradation of chemical substances in solution phase. To this aim, semiconductor photocatalysts enable a practical approach given their favorable physico-chemical properties (*e.g.* band gap values, surface-to-volume ratio). More specifically, the excellent electronic and optical properties of metal oxide materials constitute a sustainable solution for water treatment and purification as it is low-cost, green, and effective technology. Importantly, the optimization of the photocatalyst active surface-to-volume ratio [4] and the increase of its size [5] can be used to improve the efficiencies by favoring the interaction with the pollutants and decreasing the electrons-holes recombination rate. Among the metal oxide materials, ZnO is an n-type semiconductor material with a bandgap of ≈ 3.3 eV, representing an ideal choice due to its well-known photocatalytic properties, good biocompatibility as reported by the Food and Drug Administration (21CFR182.8991) [6] and versatile synthetic approaches resulting in a plethora of nanostructures with different morphology (*e.g.* nanoparticles, 1D structures or thin films), specific surface area and crystallinity. Such features are all highly relevant for the photocatalytic activity of ZnO. Among them, ZnO flower-like structures are receiving increasing interest [7–9], due to their high surface to volume ratio, versatility in preparation methods both under nano-[10] and micro-structures [11–13] also by green chemistry synthesis [14] approaches for photocatalytic decontamination and mediated amyloid degradation [15]. Nevertheless, ZnO can lead to dissolution in aqueous environments with a kinetics of the order of some hours [16], leading to the release of zinc ions in solution and unbalance the zinc homeostasis [17], eventually leading to the generation of reactive oxygen species (ROS), which can trigger apoptosis [18]. As a result, ZnO cannot be used

straightly as bare solid powders, considering that the potential leak of ions into water could be a threat but are rather prepared as composites into organic substrates polymers such as cellulose [19] or polyvinylidene fluoride-trifluoroethylene [20]. Indeed, among the polymeric materials, the well-known biodegradability [21] and biocompatibility of cellulose and its derivatives favors its employ in biomedicine and biomedical devices[22] and devices for food passive cooling [23].

Assembling the composite by out-of-equilibrium self-organization of the photocatalysts within polymeric matrices is a valid approach for enhancing their photocatalytic properties, as already shown by our group [24], given the wider landscape of the resulting physicochemical properties in comparison to those achievable under thermodynamic control [25]. ZnO flower-like structures have already been shown as active materials for composites preparation, *e.g.* PDMS for hybrid piezoelectric nanogenerators [26], photocatalytic composites based on ZnO/SnO₂-PMMA [27], cellulose-chitosan [28], and also pullulan [29]. However, there are no studies reporting on the physicochemical properties of ZnO flowers polymer composites prepared under out-of-equilibrium conditions, that correlate the photocatalytic properties with the surface-to-bulk ZnO filler loading and leakage of zinc related species in the aqueous solution where the composites are soaked.

In this work, the synthesis of a highly reusable, ZnO flowers /cellulose acetate (CA) composite films is shown. Both ZnO and CA are bactericidal and biocompatible, having been found numerous applications in biomedical sciences [22]. The ability of the composite to remove methylene blue (MB) in the dark and under solar simulation is tested, as a function of the ZnO flowers loading, in parallel Electrochemical Impedance spectroscopy (EIS) allows determining the conductivity variation of aqueous solutions in which the composites are soaked in dark conditions. The chemical composition the morphology and the thermal stability of the composites are analyzed by a comprehensive multi-technique approach.

2. Experimental

2.1 ZnO Nanostructures synthesis.

The ZnO flowers were synthesized by a rational approach at mildly basic pH[30] (85 °C, 60 h) leading to ZnO structures assembled in micrometric flower-shaped grains. The synthesis was carried out with a 250 mL solution in ultra-pure DI water with resistivity at 25 °C > 18.2 MΩ · cm (Direct-Q® 3 UV Water Purification Systems, Merck Millipore). The solution contains 15 mM zinc nitrate hexahydrate (Sigma Aldrich, ≥ 99.0%), 7.5 mM hexamethylenetetramine (Sigma Aldrich, ≥ 99.0%), 0.10 M ammonia (Alfa Aesar, 28% v/v in water), 2 mM polyethylenimine (Sigma Aldrich, average Mw ≈ 800, average Mn ≈ 600), 5 mM potassium chloride (Fluka, > 99.0%), 15 mM monoethanolamine (Sigma Aldrich, ≥ 99.0%). The precipitates at the bottom of the container are collected, washed by DI-water, dried at 60 °C for 24 h and calcined at 200 °C for 2 h. The CA/ZnO composites films were prepared from ZnO dispersed at 1-15 wt% in CA dissolved at 2 mg/mL in ethyl acetate. The dispersion is drop-casted in a 4 cm diameter beaker and placed at 80 °C for 3 h to evaporate ethyl acetate, resulting in self-standing, flexible films, with a thickness in the 30-40 μm range (see **Scheme 1** and **Figure S1**).

2.2 ZnO flowers morphological and spectroscopic characterization. UV-Vis diffuse reflectance spectra on the ZnO flowers were recorded by using a UV-Vis-NIR V-770 Jasco spectrophotometer equipped with a 60 mm integrating sphere (ISN-923). ZnO flowers powder was placed in the solid sample holder, and measurements were performed in the range 200-800 nm by setting a scan speed of 100 nm/min and a bandwidth of 2 nm. The photocatalyst band gap was calculated by means of the Kubelka-Munk method [31]. UV-Vis spectra in transmission mode were recorded in the 200 nm to 600 nm range with steps of 0.2 nm using a UV-VIS spectrometer

ONDA TOUCH UV-21. X-ray diffraction (XRD) data were acquired by a Rigaku Smartlab SE XRD multipurpose diffractometer, using a Cu K α radiation source ($\lambda = 0.154$ nm), run at 40 kV and 50 mA.

The ζ -potential experiments were performed by Zetasizer Nano-ZS (Malvern Instruments) under isothermal conditions at 25 °C. The measurements were carried out using a disposable folded capillary cell on an aqueous dispersion of ZnO (0.5 mg mL⁻¹). The resulting pH of the dispersion was measured by using the Eutech pH 700 pH meter (Eutech Instruments Europe B.V., Landsmeer, Netherlands).

The morphology of the CA/ZnO samples was examined using a TESCAN MIRA 3 field emission scanning electron microscope (FE-SEM, TESCAN, Brno, Czech Republic) equipped with an energy dispersive X-ray (EDX) spectrometer (OXFORD XPLORE 30). For both imaging and EDX analysis, the FE-SEM was operated at 30 keV electron energy and 1 nA beam current. The working distance was set to 8 mm during image acquisitions and to an analytical distance of 15 mm during EDX analysis. To avoid image distortion due to sample charging and beam-induced damage, a ≈ 25 nm Al conductive coating was deposited on sample surface by thermal evaporation. Al was also an effective choice to get semi-quantitative and reproducible data by EDX, since the characteristic X-ray peaks of Al do not overlap with those of C, O, and Zn. For each sample, i.e., the pure CA and the CA samples loaded with 1 wt%, 5 wt%, 10 wt%, and 15 wt% ZnO, morphological and EDX analyses were performed on both the top and bottom sides. Optical images of the sample were acquired in Transmission Mode using a Leica SP5 confocal microscope. The CA/ZnO film was deposited onto a coverslip (Brand #1), adding 50 μ L of water to prevent optical mismatch. Images with a resolution of 1024 \times 1042 pixels were acquired using a 63 \times Leica objective (NA = 1.4) and a white light laser ($\lambda = 520$ nm).

The wettability of CA based films was studied through a contact angle apparatus (OCA 20, Data Physics Instruments) equipped with a video measuring system having a high-resolution CCD camera. The contact angle (θ) of water in air was measured by the sessile drop method at 25.0 ± 0.1 °C.

Fourier-transform infrared (FTIR) spectra were recorded using a single beam FTIR spectrometer (FT/IR-4X, Jasco Corp.) coupled with the ATR-PRO4X (ZnSe prism) single reflection accessory with an angle of incidence of 45° and contact area with diameter of 2.5 mm. The scan range was set to $500\text{-}4000$ cm^{-1} , with an accumulation of 20 and a wavenumber resolution of 1 cm^{-1} .

The XPS analysis was carried out by the PHI 5000 VersaProbe II scanning microprobe (ULVAC-PHI). Spectra were acquired using a monochromatic Al $K\alpha$ radiation ($h\nu = 1486.6$ eV), 100 μm diameter beam (25 W, 15 kV); electrons were collected at 45° and 90° with respect to the surface and analyzed with a hemispherical analyzer operating in FAT mode.

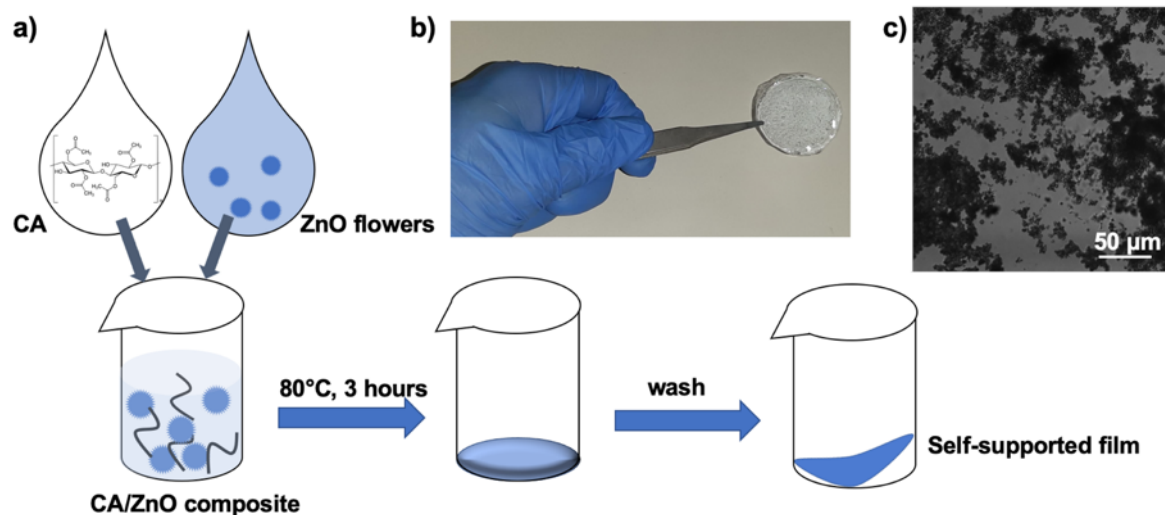
Thermogravimetric analyses were conducted by using a Q5000 IR apparatus (TA Instruments) under inert atmosphere. To this purpose, Nitrogen flows of 25 and 10 cm^3 min^{-1} were employed for the sample and the balance, respectively. The sample mass was ca. 5 mg for each measurement. The sample was heated from room temperature to 600 °C by a scanning rate of 20 °C min^{-1} .

2.3 Photocatalytic characterization. The photocatalytic activity of the samples (size 20 mm x 10 mm, thickness evaluated by the optics of the Nano eNabler Molecular Printing System from BioForce Nanoscience, USA) was evaluated by the photodegradation of MB in aqueous solution (3 mL, 25 μM). Irradiation was carried out using the Model 10500 ABET Low Cost Solar Simulator (Abet Technologies, USA) equipped with a 150 W Xenon arc lamp and an AM1.5 G filter. The distance between the sample and the solar simulator was set using a calibration cell commercial KG5-filtered Si calibration cell (model 15151, Abet Technologies, USA) to obtain an

incident light power of $100 \text{ mW} \cdot \text{cm}^{-2}$, corresponding to 1 sun. Control experiments were conducted in dark. Before light irradiation, samples were soaked into the MB solution in the dark for 1 h to permit adsorption-desorption equilibrium. Irradiation effects were evaluated at 30 min intervals by analyzing changes in the absorption spectra of the MB solution. Spectra were acquired using a UV-Vis spectrophotometer (Specord S600, Analytik Jena, Jena, Germany), in the range 400-800 nm, with a wavelength accuracy of $\pm 0.3 \text{ nm}$. Intensity measurements at 664 nm were permitted to quantify spectral changes. Control experiments were carried out by monitoring the MB solution concentration decrease in the absence of irradiation. The reusability was tested by repeating the cycles of MB solution photodegradation on the same sample. The reproducibility was investigated by replicated photocatalysis experiments on three different samples.

2.4 Electrochemical analyses. The electrochemical characterizations were carried out by employing a potentiostat/galvanostat instrument (Metrohm Autolab PGSTAT 128 N, Utrecht, Netherlands). Anodic stripping voltammetry detection of zinc ions released by the CA/ZnO (10 wt%) film under dark or light irradiation, were carried out by employing a 3-electrodes serigraphic sensor (ItalSens-Au sensor, Houten, Netherlands), based on a previously reported protocol [32]. In brief, a reduction potential of -0.9 V was applied for 90 s without stirring for Zn^{2+} ions pre-concentration (step potential: 4 mV; amplitude: 50 mV, frequency: 50 Hz) in a 0.1 M Britton-Robinson buffer (pH 7.0) as the background electrolyte. The buffer was prepared from acetic acid (Sigma Aldrich, ReagentPlus $\geq 99\%$), boric acid (Sigma Aldrich, BioReagent $\geq 99.5\%$) and orthophosphoric acid (Sigma Aldrich, 85 wt% in H_2O) and the pH (Eutech Instruments Europe B.V.) was adjusted to 7.0 with NaOH (0.1 M Merck). The measurements were conducted by diluting 20 μL into 180 μL of the 0.1 M Britton-Robinson buffer. Zinc leakage was evaluated under irradiation and in the dark at 30 min intervals by analyzing changes in the peak current

spectra due to the anodic stripping of the zinc ions. Electrical Impedance spectroscopy (EIS) measurements were carried out by employing a 3-electrodes serigraphic sensor (ItalSens IS-C) in the frequency range comprised between 1 kHz and 5 MHz, wave amplitude 10 mV at 0 V bias. The measurements were conducted directly on the ultrapure water media in which the samples were loaded.



Scheme 1. (a) Scheme for the realization of the CA/ZnO films obtained by mixing ZnO flowers and cellulose acetate in ethyl acetate. After solvent evaporation, self-standing flexible film is obtained as show in (b) optical photograph and (c) microscopic characterization showing the ZnO flowers dispersed in the CA polymeric matrix at 1 wt%.

3. Results and discussion

3.1 Chemical characterization of the ZnO flowers

The crystallinity of the ZnO flowers and their bandgap were determined (see **Figure 1**). XRD measurements (Figure 1a) allowed to obtain diffraction peaks of ZnO at 31.9°, 34.1°, 36.4°, 47.9°, 56.6°, 61.6°, 66.1°, 67.3°, 68.9°, 72.2° and 76.6°, corresponding to (100), (002), (101), (102), (110), (103), (200), (112), (201), (004) and (202) which are all in accord with the hexagonal wurtzite ZnO, ICDD card no. 36-1451 without impurity crystalline phases [33]. The obtained results well agree

with previous reports on ZnO flower like structures [28], in which the growth orientation of ZnO nanoparticles along the (100) direction was enhanced and the obtained ZnO exhibited plate-like systems [34] lacking a preferential orientation along the c-axis which is typical of ZnO nanorods [35]. Such preferential (100) direction is associated with improved photocatalytic activity with respect to the (002) direction [36]. The following reticular parameters were obtained: $c = 5.231$ $a = 3.263$, associated to a hexagonal cell unit. The crystallite domain sizes by the Scherrer formula [37] for the seedless and seeded samples were equal to 15.1 nm, 17.4 nm and 14.4 nm for (100), (002), and (101).

The optical band gap of the ZnO flowers was calculated through diffuse reflectance measurements. In Figure 1b, the reflectance spectrum of ZnO powder shows a high value of reflectance in the whole visible part of the spectrum (400-800 nm), while a decay of the signal was observed for wavelengths above 400 nm in the UV range. By the reflectance spectrum of ZnO powder, it was possible to calculate the band gap energy by using the Kubelka–Munk method [31]. By the Kubelka–Munk method, the diffuse reflectance spectrum is transformed in the plot of $[F(R)hv]^n$ versus the incident photon energy. The band gap value is obtained as the intercept of the extrapolation of the linear portion of curves to zero on the x-axis (**Figure S2**). The method allowed to obtain a band gap energy of 3.17 eV, which corresponds to 390 nm, in accordance with previously reported values for ZnO-based materials [5]. The ζ -potential of the ZnO was equal to $-27.3 \text{ mV} \pm 0.2 \text{ mV}$, demonstrating a quite good stable dispersion (whose pH is around 7.74), owing to the negative charge. This value is in good agreement with previous reports on ZnO flowers [37].

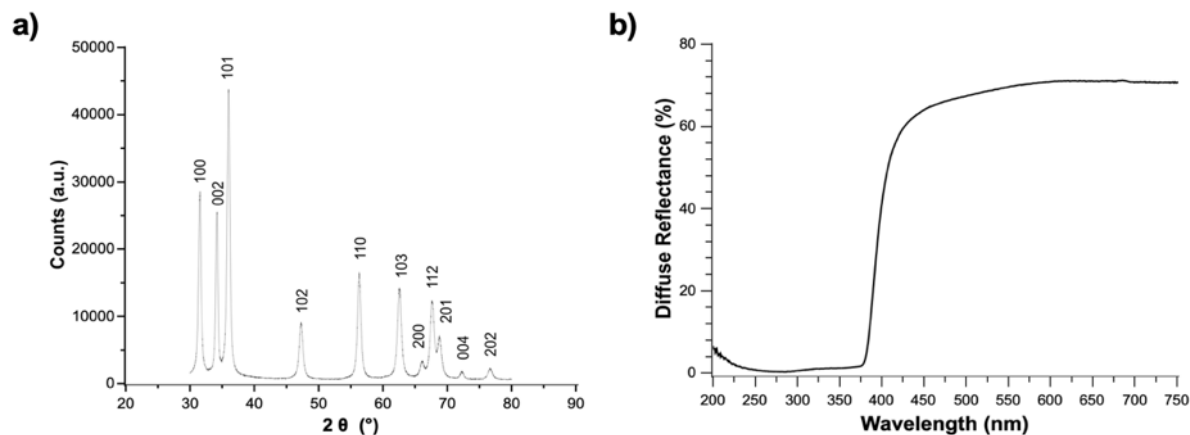


Figure 1. (a) XRD characterization of the ZnO flowers showing the expected diffraction peaks of ZnO and (b) DRS measurement permitting to estimate the energy bandgap.

3.2 Morphological characterization of CA/ZnO composites films

The structural and morphological characterization by SEM analysis of the pure CA sample and CA samples loaded with different concentrations of ZnO flowers is reported in **Figure 2**. SEM images of both the top and bottom sides, recorded at two different magnifications (namely, 200× and 2k×), are displayed for each sample. SEM images of the pure ZnO powder and high magnification images from the bottom side of the 15% ZnO loaded sample are shown in the Supplementary Information (**Figures S3** and **S4**, respectively). Pure CA exhibits a nearly featureless morphology and a smooth surface both on the top (Figure 2a) and bottom side (Figure 2b). As for the latter, some particulates related to unwanted contamination are visible at low magnification. SEM images from the top sides of CA samples loaded with 1 wt%, 5 wt%, 10 wt%, and 15 wt% ZnO (Figures 2c, 2e, 2g, and 2i, respectively) show denser light stains due to the higher concentration of ZnO structures embedded in the CA matrix. Higher magnification images of top sides clearly show the morphology of ZnO inclusions dispersed in CA, in the form of ZnO flowers and also some ZnO nanowire. The bottom sides of the 1 wt%, 5 wt%, 10 wt%, and 15 wt% ZnO loaded samples (Figures 2d, 2f, 2h, and 2j, respectively) show a markedly different topography with respect to the top sides. As expected, for

both the evaluated magnifications, the higher the concentration of ZnO embedded in the CA matrix, the higher the coverage of ZnO onto the CA surface. The morphological differences between the top and bottom sides of the ZnO loaded samples reasonably indicate a sedimentation of ZnO nanostructures in the CA matrix during the drying process.

The results of EDX analysis in terms of weight% and atomic% elemental compositions performed on both the top and bottom sides of the pure CA and 1 wt%, 5 wt%, 10 wt%, and 15 wt% ZnO loaded CA are summarized in **Table 1**. The reported values are the average over three different recordings for each examined sample. As expected, both sides of the pure CA sample exhibit the same amount of carbon and oxygen, with no detected amount of Zn. Elemental composition of top sides of ZnO loaded CA samples shows increasing amounts of Zn as nominal Zn concentration increases, however, accordingly to SEM images, it is clearly influenced by the screening effect of the bulky CA embedding ZnO. On the contrary, EDX data taken from the bottom sides show increasing amounts of Zn, both Wt% and at%, in good agreement with the nominal variations in Zn concentration. These variations are well displayed in **Figure 3**, where the EDX maps of elemental distributions of C, O, and Zn for the bottom sides of the pure CA and the ZnO loaded CA are displayed respectively in Figure 3a, 3b and 3c.

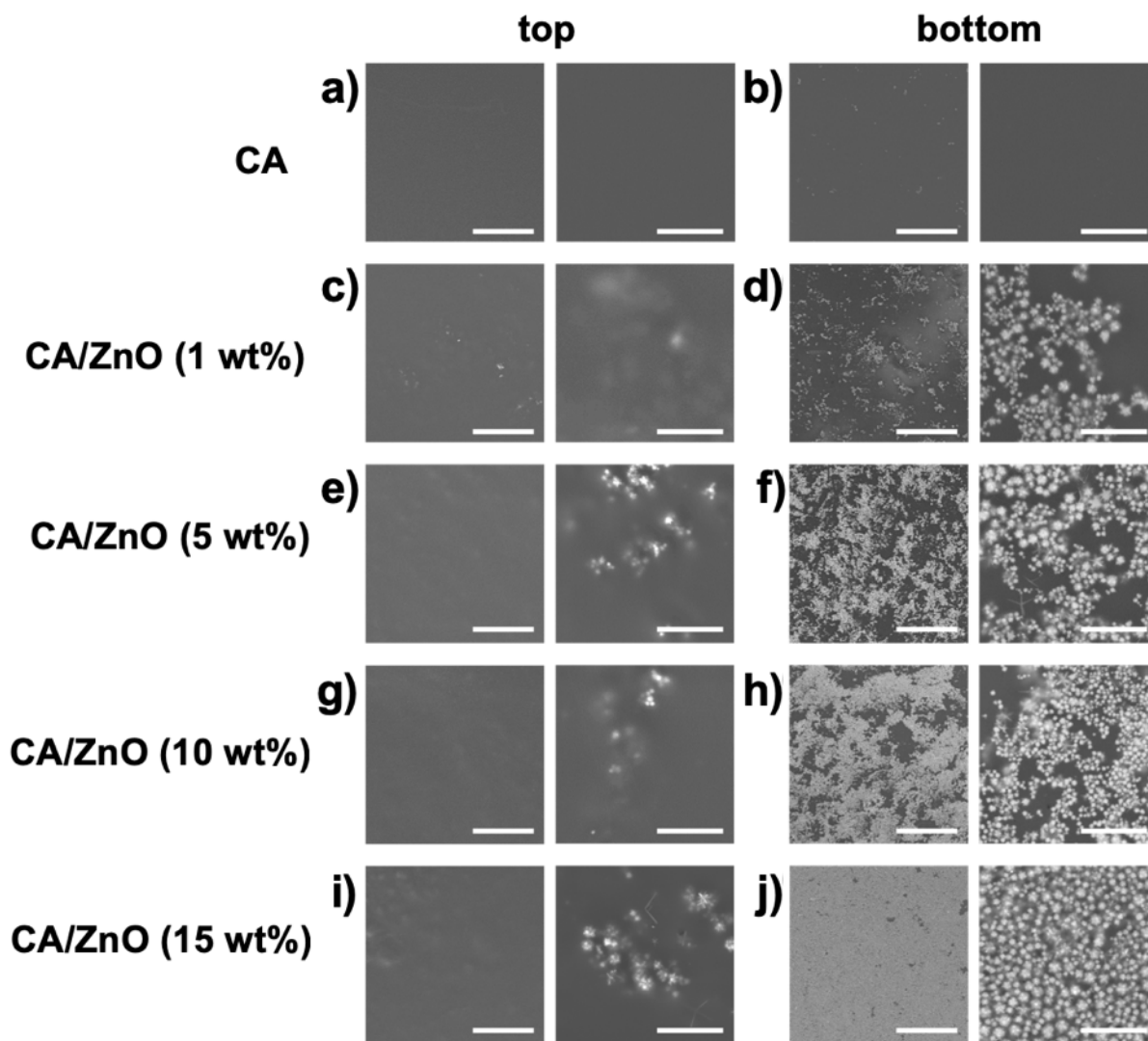


Figure 2. Top-view SEM images of top and bottom sides of **(a)** and **(b)** pure CA, respectively; **(c)** and **(d)** CA loaded with 1 wt% ZnO; **(e)** and **(f)** CA loaded with 5 wt% ZnO; **(g)** and **(h)** CA loaded with 10 wt% ZnO; **(i)** and **(j)** CA loaded with 15 wt% ZnO. SEM images taken at two different magnifications, namely 200x and 2kx, are displayed in left panels (scale bars 200 μm) and right panels (scale bars 20 μm).

	top		bottom	
	Wt%	at%	Wt%	at%
pure CA				
Zn	--	--	--	--
O	45.16	38.20	45.17	38.22
C	54.84	61.80	54.83	61.78
1 wt%	Wt%	at%	Wt%	at%
Zn	0.11	0.02	3.55	0.75
O	45.21	38.29	41.54	35.94
C	54.68	61.69	54.91	63.31
5 wt%	Wt%	at%	Wt%	at%
Zn	0.16	0.03	12.93	2.94
O	45.58	38.66	34.36	31.90
C	54.26	61.31	52.71	65.16
10 wt%	Wt%	at%	Wt%	at%
Zn	0.21	0.04	20.16	4.9
O	43.92	37.10	31.16	30.86
C	55.87	62.86	48.68	64.24
15 wt%	Wt%	at%	Wt%	at%
Zn	0.34	0.07	30.71	8.25
O	44.20	37.41	26.33	28.92
C	55.46	62.52	42.96	62.83

Table 1. EDX Elemental Analysis of CA/ZnO composites at different ZnO wt% loadings.

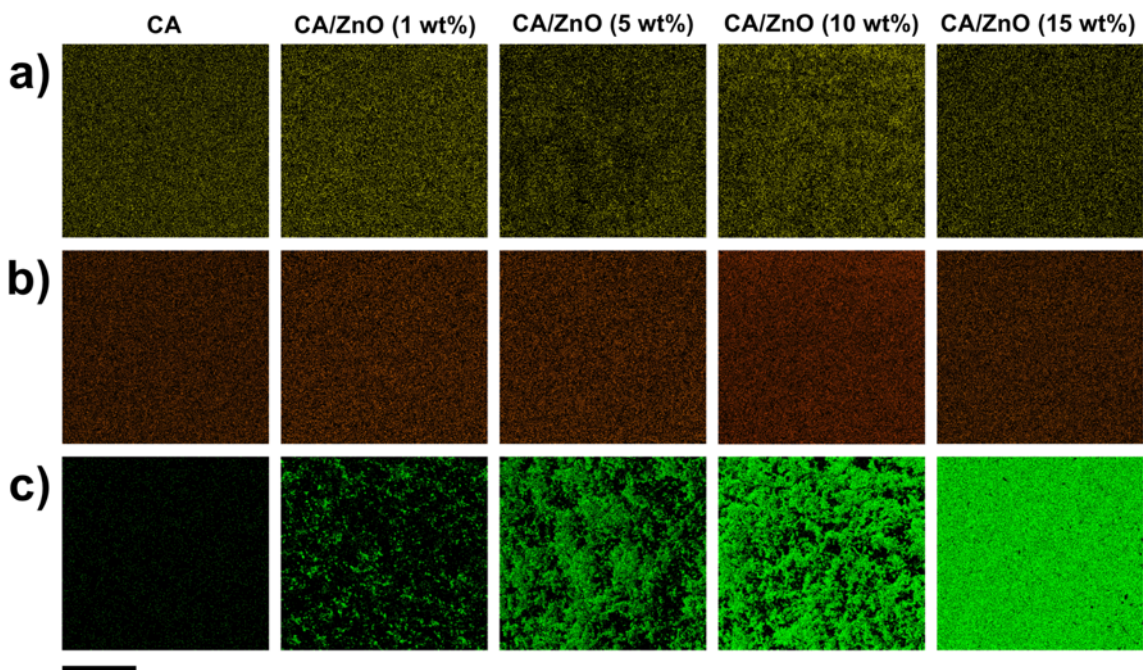


Figure 3. EDX maps of elemental distributions of (a) C, (b) O, and (c) Zn at the bottom sides on the same scan area (scale bar 500 μm) for pure CA, 1 wt%, 5 wt%, 10 wt%, and 15 wt% ZnO loaded CA (panels from left to right).

3.3. Chemical characterization of the composites

FTIR analysis was used to investigate the dispersibility and the chemical interaction between cellulose acetate and ZnO. The spectra of ZnO flowers powder, pure CA, and CA blended with 10 wt% ZnO analyzed by FTIR are shown in **Figure 4**. The FTIR spectrum of the ZnO powder shows a strong absorption toward 500 cm^{-1} , corresponding to the $426\text{--}565\text{ cm}^{-1}$ absorption bands of the Zn–O stretching vibration of wurtzite hexagonal structured Zn–O crystal [38],[39].

A weak peak centered at 890 cm^{-1} and a very weak band in the region $3350\text{--}3550\text{ cm}^{-1}$ can be assigned to –C–H bending vibrations and to stretching vibrations of O–H groups, respectively [40]. The former is presumably due to residue of ethanol used during processing of ZnO powders, whereas O–H groups can be related to a negligible amount of absorbed water molecules hydrogen bonded to the ZnO surface [39],[40]. The pure CA shows the characteristic peaks of cellulose acetate [41–44].

Specifically, a wide band in the 3600-3300 cm^{-1} region, with a peak at about 3475 cm^{-1} , can be assigned to the stretching of intermolecular hydrogen bonds of hydroxyl groups (O–H) and contains contributions from both adsorbed moisture and the hydroxyl groups of non-esterified cellulose. The weak peaks located at 2950 cm^{-1} and 2890 cm^{-1} correspond to the stretching of CH of methyl groups (–CH₃) and to the CH₃ symmetric stretching, respectively. The intense absorption peak at 1733 cm^{-1} is attributed to the stretching vibration of the carbonyl group (C=O), and the characteristic peaks at 1215 cm^{-1} and 1028 cm^{-1} can be related to the antisymmetric and symmetric C–O–C stretching modes of the ester group, respectively. The peaks at 1368 cm^{-1} and 1432 cm^{-1} correspond to the symmetric CH₃ bending and to the CH₂ deformation, respectively. Finally, the absorption peak at 900 cm^{-1} is assigned to acetate methyl groups. As regards the CA/ZnO composite, some changes in the FTIR spectrum of the pure CA arise upon addition of ZnO flowers [45–49]. The presence of ZnO in the 10 wt% ZnO composite film causes the appearance of a strong absorption toward 500 cm^{-1} , due to the Zn–O stretching vibrations. The characteristic peaks of the pure CA are found almost unchanged in the FTIR spectrum of the CA/ZnO composite, apart the hydroxyl group band, which is significantly broadened toward lower wavenumbers, as shown in the deconvolution analysis displayed in **Figure S5**. As suggested in previous studies [47,48,50], this can be related to the formation of hydrogen bonding between ZnO and CA, which is a further confirmation of the successful incorporation of CA with ZnO. Finally, **Figure S6** shows the UV-VIS absorption spectra for cellulose acetate (CA) and CA loaded with different concentrations of ZnO (1 wt%, 5 wt%, 10 wt%, 15 wt%). The absorption spectrum of CA is almost flat in the 250-600 nm range, with an absorption onset at about 240 nm.[51] Instead, an absorption peak at around 378 nm (\approx 3.28 eV) can be clearly observed in all ZnO loaded CA samples, which is consistent with exciton absorption peaks observed for different ZnO nanostructures, with a blue-shift from that of bulk ZnO (380 nm) [52].

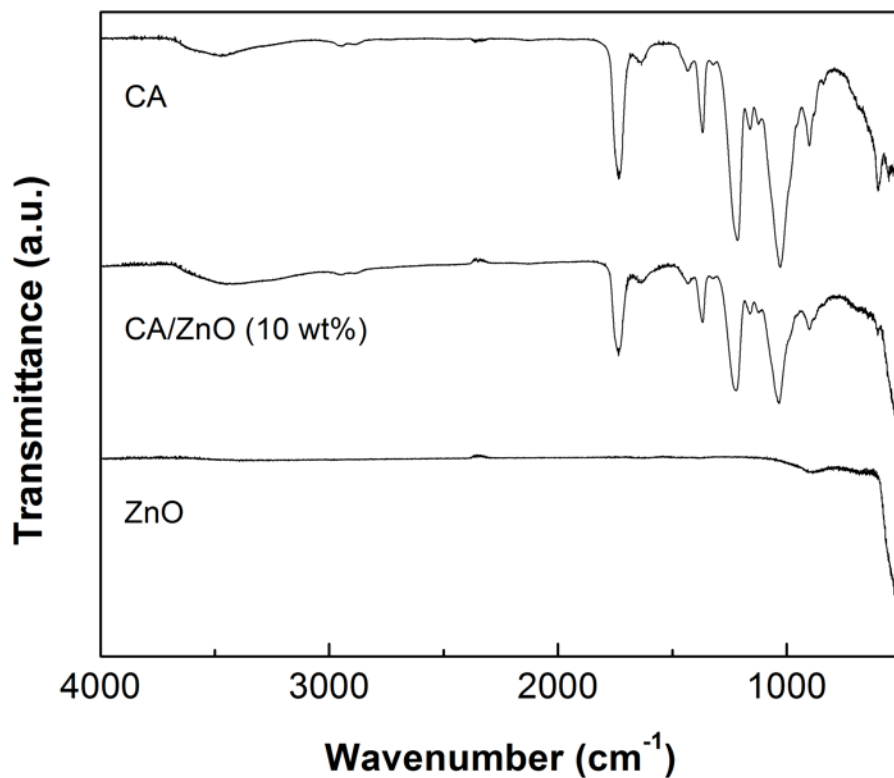


Figure 4. Fourier transform infrared spectroscopy (FTIR) spectra of ZnO powders, pure cellulose acetate (CA), and cellulose acetate loaded with 10 wt% ZnO in the range 500-4000 cm⁻¹.

The influence of the ZnO addition on the wettability surfaces of CA based films was investigated by water contact angle experiments. **Figure 5** shows the images and the corresponding contact angle values of the water droplets immediately after their deposition on both sides of the films.

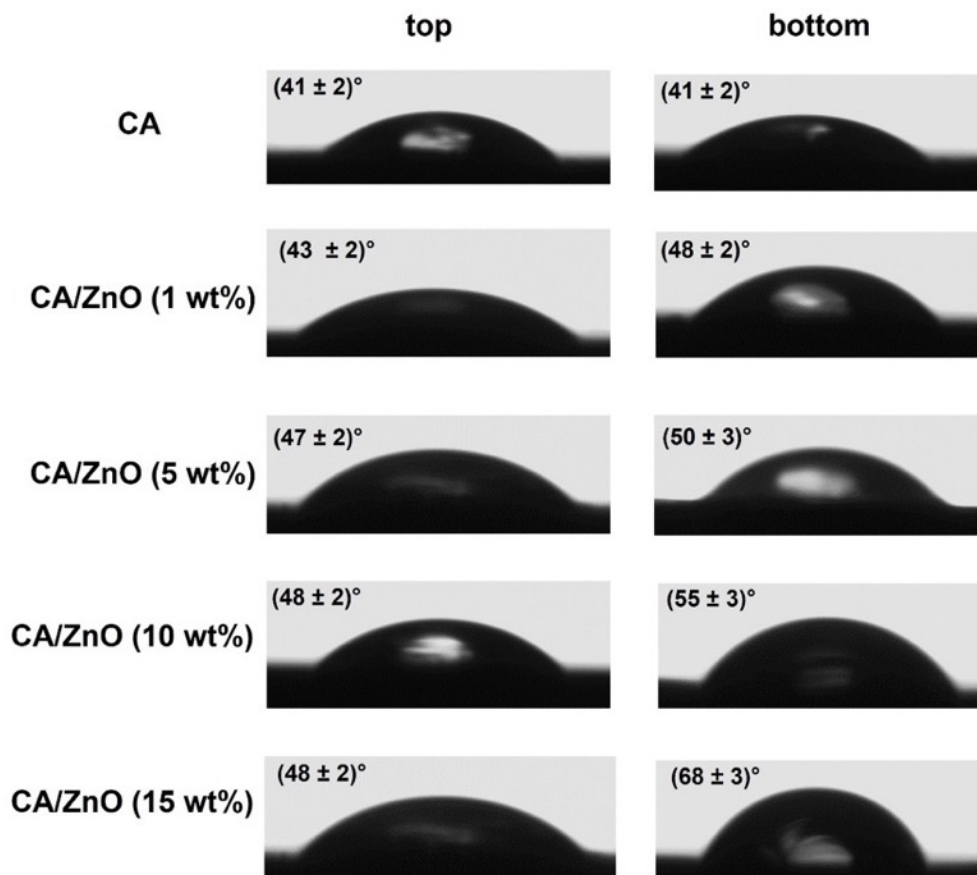


Figure 5. Images of the water droplets immediately after their deposition on the CA based films with variable ZnO content. The corresponding contact angle values are presented.

The initial water contact angle (ca. 41°) of pristine CA agrees with the hydrophilic nature of the polymer. As expected, the wettability characteristics of the film based on CA are similar on both top and bottom surfaces highlighting the homogeneity of the sample. As a general result, the filling of the polymeric matrix with ZnO generated an enhancement of the initial water contact angle evidencing a hydrophobization effect of the fillers on the CA based film. According to literature [53,54], the addition of ZnO can determine the hydrophobization of polymeric films because of roughness increase as well as variations of the surface chemical composition. Within this, SEM/EDX analyses evidenced that the CA based films possess variable roughness and surface chemistry on dependence of the ZnO content. In addition, it should be noted that the employed synthesis protocol

produces hydrophobic ZnO flowers mainly exposing apolar planes as evidenced by XRD analysis, ultimately enhancing the surface hydrophobization effect[55] on the polymeric films, proportionally to the nanofiller content of the CA/ZnO composites for both sides. Nevertheless, it is remarkable to note that the hydrophobization effect is significantly stronger for the bottom side of the film surface. This finding agrees with SEM images (**Figure 2**), which showed that the coverage of ZnO nanostructures onto the CA surface is higher for the bottom surface.

XPS characterization of the CA/ZnO (10 wt%) sample highlights that complete absence of zinc from the top surface (**Figure S7**), being only a minimal quantity (0.28 at%) detectable at the bottom surface of the same sample. These data well agree with the EDX and SEM characterizations. The quantitative analysis of the carbon relative species at the top surface was carried out by the analysis of the C 1s spectra and the resulting fitting of the peak at 45° and 90°, as shown in (**Figure 6**).

When collecting XPS spectra, the sampling depth is determined by the takeoff angle (θ) and the inelastic mean free path (IMFP), in the relation of $\text{depth} = \text{IMFP} \sin \theta$. By sampling at two different angles, the collected data at 90° collect and average data from all the IMFP depth – about 10 nm – while at 45° we sample about 7 nm. The comparison (see Table 2) shows a significant decrease in the relative abundance of alkylic signal going from 45° to 90°, indicating a superficial segregation of hydrophobic (alkylic) species.

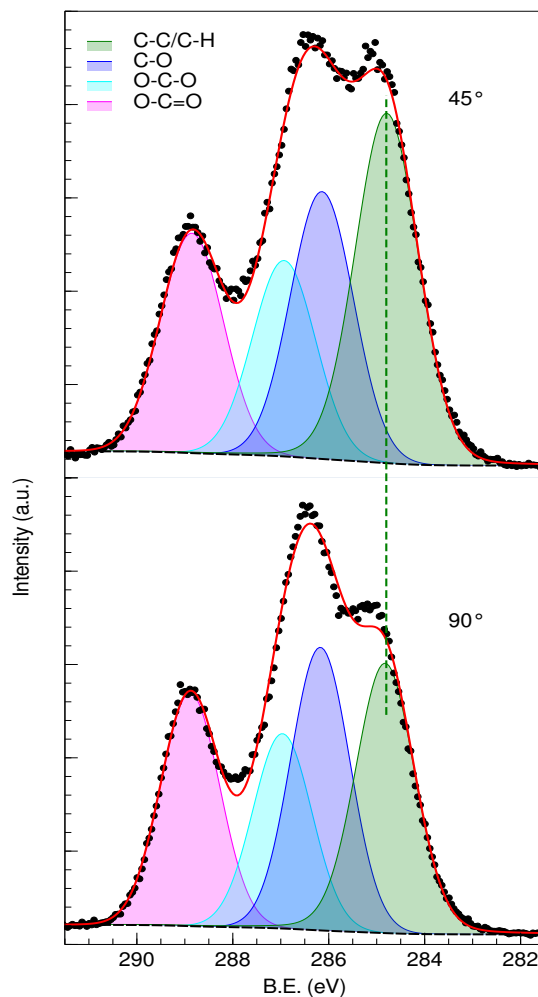


Figure 6. Analysis of the C 1s peak signal obtained from the top surface of the CA/ZnO (10 wt%) sample taken at 45° (top) and 90° (bottom) electron takeoff angles.

	C-C/C-H	C-O	O-C-O	O-C=O
45°	34.73	25.54	18.72	21.01
90°	28.54	28.45	19.58	23.43

Table 2. Atomic percentage distribution of carbon species derived from C 1s peak analysis from the top surface of the CA/ZnO (10 wt%) sample.

3.4 Thermal characterization

Figure 7 shows the thermogravimetric (TG) curves of pristine and ZnO loaded CA composites with variable filler contents (1 wt% and 10 wt%).

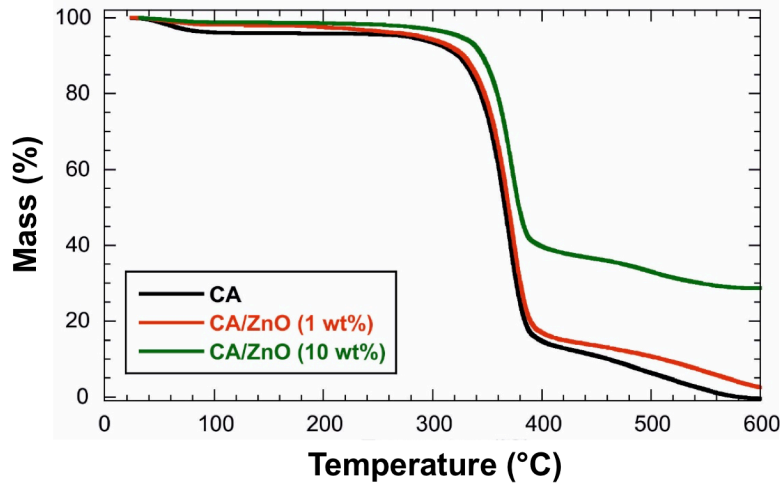


Figure 7. Thermogravimetric curves of CA based films filled with variable amounts of ZnO.

The analysis of TG curves allowed the estimation of the water content of the films by determining the mass losses from 25 °C to 150 °C (ML_{150}). As reported elsewhere [56], the ML_{150} values reflect the water molecules physically adsorbed onto both inorganic and organic materials. We detected that the ZnO addition reduces the ML_{150} value (**Table 3**) highlighting that the nanocomposites possess a lower hydrophilicity compared to pristine CA.

Film	ML_{150} / wt%	MR_{600} / wt%	T_{ons} / °C
CA	4.19 ± 0.06	0	332 ± 3
CA/ZnO (1 wt%)	2.09 ± 0.04	2.46 ± 0.04	338 ± 3
CA/ ZnO (10 wt%)	1.36 ± 0.03	28.6 ± 0.6	347 ± 3

Table 3. Thermogravimetric parameters of CA based films.

As a general result, TG curves evidenced a relevant mass loss between 280 °C and 420 °C, which represents the temperature range of CA pyrolysis. Accordingly, we determined the polymer decomposition temperature from the onset point of TG curve within the mentioned interval. Interestingly, the onset temperature (T_{ons}) is larger for CA/ZnO composites with respect to that of pristine polymer. On this basis, we can state that ZnO induces a thermal stabilization effect on the polymer that might be attributed to the barrier effect of the nanofillers towards the volatile products

generated by the CA decomposition. The polymer thermal stabilization depends on the ZnO concentration as evidenced by the T_{ons} increases (6 °C and 15 °C at 1 and 10 wt%, respectively) with respect to the film based on pristine CA. Furthermore, pristine CA presents a null residual mass at 600 °C (MR_{600}). This result indicates that the polymer is completely decomposed at 600 °C. Oppositely, CA/ZnO composites did not exhibit a complete decomposition at 600 °C as evidenced by their MR_{600} values (2.46% and 28.6% at 1 and 10 wt%, respectively). This thermal behavior can be related to the addition of inorganic fillers (ZnO flowers) that are stable at high temperatures.

3.5 Photocatalytic activity

The formation of ROS under simulated solar light is demonstrated by the photocatalytic degradation of the dye methylene blue (MB), monitored from the absorption spectra of the MB solution (3 mL, concentration C_i equal to $2.5 \cdot 10^{-5}$ M) into which CA/ZnO composites were soaked (see **Figure 8** and **Figure S8**). As shown in Figure 8, a scarce MB adsorption is observed for all the samples, being significant only for highest ZnO loadings in the cellulose matrix (10-15 wt%). Under irradiation by the solar simulator, ZnO loading in the polymer matrix increases the MB degradation, as expected (Figure 8a). Control experiments in the absence of light show a scarce but still quantifiable decrease in MB concentration (Figure 8b). Notably, the photocatalytic activity increases from 1 wt% to 10 wt% ZnO loading, observing a decrease at 15 wt%. This observation can be ascribed to the interplay between the beneficial effect on photodegradation and their induced decrease on the MB adsorption, which is shown by the increase of the contact angle both in the top and especially at the bottom face of the composite by the increase of ZnO loading. The photocatalytic degradation rate can be modelled using a pseudo-first-order kinetics. It was possible to determine an apparent rate constant (k) by the linear regression model $\ln(C/C_0) = kt$, in which C is the MB concentration after a given time exposure at 1 sun irradiation time and C_0 is the concentration after adsorption/desorption equilibrium. The

resulting apparent reaction constant k increases as a function of the ZnO loading, showing an apparent optimal degradation kinetics of $0.020 \text{ min}^{-1} \pm 0.001 \text{ min}^{-1}$ (at 10 wt%), along with an excellent reusability at the second and third cycles, being equal to $0.039 \text{ min}^{-1} \pm 0.001 \text{ min}^{-1}$ and $0.039 \text{ min}^{-1} \pm 0.002 \text{ min}^{-1}$, respectively (see **Table S1**). An increase of the photocatalytic efficiency for all the investigated ZnO loadings was observed at the second use. This could be ascribed to adsorbed MB molecules on the composite surface or into its bulk which were washed before the second use. Another possible explanation is the swelling of cellulose acetate polymeric matrix that favors MB adsorption in the composite, as shown by the higher adsorption of the reused samples at all the investigated ZnO loadings. Notably, the photodegradation third cycle is similar to the one of the second cycle, suggesting the good reusability of the composite in real applications and further suggesting that the ZnO flowers are stabilized in the cellulose matrix even after multiple photodegradations (Figure 8c), in accord with previous studies dealing with ZnO/SnO₂-PMMA composites [27]. The 10 wt% loading showed, similarly to the experiments carried out in the presence of light, the best results, leading to a decrease of about 7% of MB concentration. This behavior is likely due to the ZnO loading which negatively affects the composite wettability at high concentrations higher than 10 wt% MB photodegradation reproducibility was also evaluated on three different CA/ZnO (10 wt%) samples which showed very similar photodegradation efficiencies, equal to 96%, 93% and 96%. The obtained values are among the best if compared with previous results considering ZnO composites with cellulose-based materials (**Table S2**).

A part from the light-triggered induction of ROS species, CA/ZnO can release of Zn²⁺ ions under dark and solar light illumination [57]. To this aim, Zn²⁺ ions leaked from the sample showing optimal photocatalytic properties - i.e. CA/ZnO (10 wt%) - was evaluated by voltammetry [32] in the absence and in the presence of light (Figure 8d and **Figure S9**). As can be seen, solar light induced a

significant increase (almost 5-fold at the end of the 2 h irradiation) of the zinc ions leakage into the solution in which the composites are immersed, as a result of the photoinduced process of ZnO flowers surface degradation, that is ascribed to the photo-generated holes on ZnO surface that could attack the Zn–O bond and as a result disassociate the Zn^{2+} from the ZnO surface.[58] Considering the calibration reported in **Figure S10**, it is possible to estimate the leaked zinc ions species at the $1.5 \text{ ppm} \pm 0.2 \text{ ppm}$ and $7.0 \text{ ppm} \pm 0.9 \text{ ppm}$. Interestingly, the zinc release follows a linear trend as a function of time, in agreement with a zero-order kinetics release mechanism, with an apparent kinetics constant equal to $0.098 \text{ } \mu\text{A}/\text{min} \pm 0.007 \text{ } \mu\text{A}/\text{min}$. The observed trend of the CA/ZnO (10 wt%) composites is significantly different from the complex behaviors reported on ZnO powders with different shapes and surface-to-volume ratios [59,60], opening up towards higher controllability in light-triggered zinc ions release.

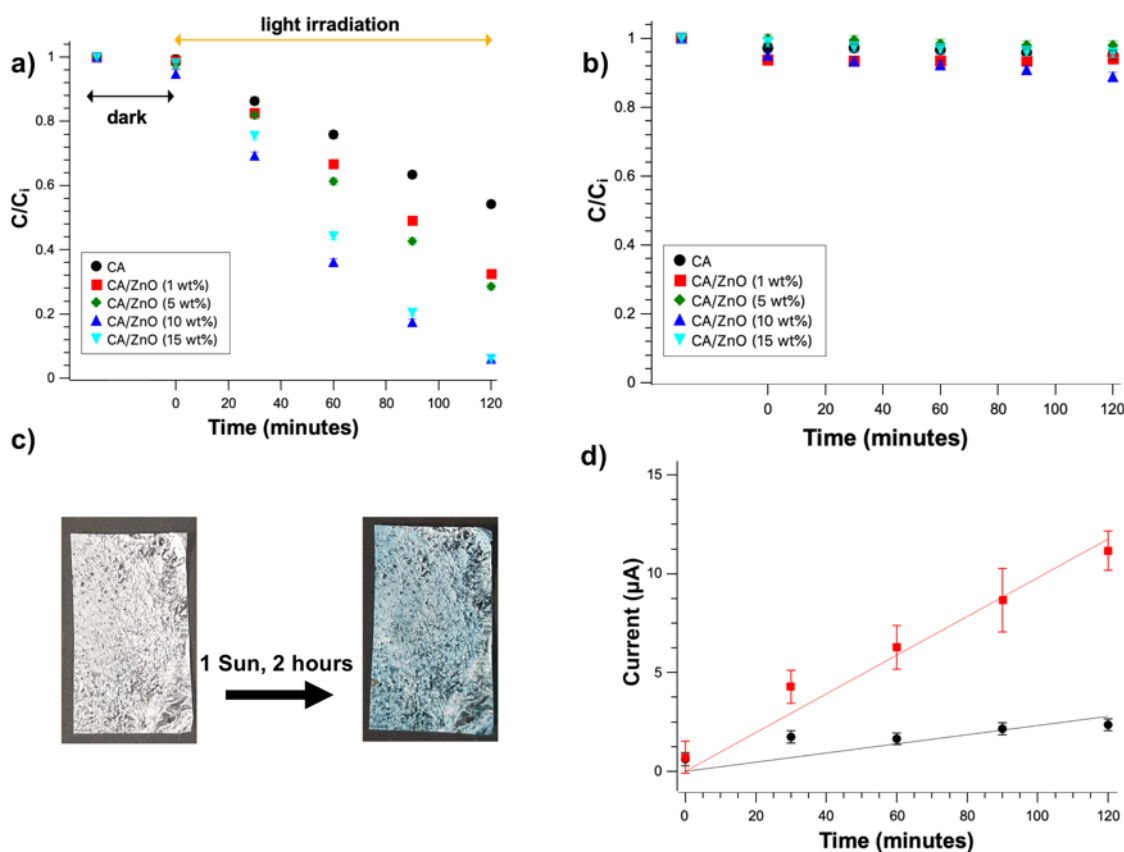


Figure 8. (a) Photodegradation of MB vs time in CA/ZnO composites: bare CA (black squares), 1 wt% (red squares), 5 wt% (green circles), 10 wt% (triangles), and 15 wt% (light-blue triangles). (b) Control experiment conducted in the absence of light-induced degradation shows dim decrease of MB vs. time. (c) Photograph of CA/ZnO composites after a typical photocatalytic cycle. (d) Voltammetric analysis of Zinc ions release from the CA/ZnO (10 wt%) composite in the absence (black dots) and presence (red squares) of irradiation.

3.6 CA/ZnO flowers composites analysis in dark conditions

The overall leakage of zinc and cellulose related species from CA/ZnO composites was further analyzed under dark conditions (i.e. in the absence of solar light) through EIS on screen printed sensors, leveraging microfabricated electrodes to use sub-milliliter sample volume [61]. Microfluidic chips allow direct ROS quantification from blood impedance [62,63] or even for the determination of hydroxyl radicals produced from living cells [64]. In particular, ZnO can produce zinc ionic related species by a dissolution mechanism into the aqueous media mediated by the presence of the cellulose acetate matrix. To demonstrate this, composite samples at different ZnO loading were soaked in ultrapure water (2 mL) and the impedance of the solution was measured from the same day up to four days after immersion. The Bode plot of the water CA/ZnO composites were acquired on the ultrapure water after immersion (**Figure S11**). The typical impedance values (Z) extracted at the kHz range represents a usable value for applications in biointerfaces, but at this frequency capacitive effects are present in addition to resistive ones [61]. Also, values at frequency higher than 10^4 Hz might be affected to instrumental artifacts [65]. Accordingly, from the Bode plots, a capacitive and then a frequency-dependent regions are both at low ($< 3 \cdot 10^3$ Hz) and high ($> 5 \cdot 10^4$ Hz), presenting an essentially frequency independent response at intermediates frequencies, being mainly ascribed to the solution conductivity [61]. Thus, the comparison among the different samples was conducted confronting the impedance in the frequency independent region at the $5 \cdot 10^3$ Hz frequency, at which the impedance contribution is mainly due to the solution conductivity. As expected, the higher the

ZnO filler concentration, the lower is the Z values with respect to the one of the bare CA sample during the four days monitoring, as a possible effect of ionic zinc related species release, in agreement with the observation of Zn^{2+} release in dark conditions. The decrease of the Z values is normalized with respect to the value measured for CA sample (**Figure 9**). Unexpectedly, CA induced a significant reduction of Z with respect to the control sample consisting in ultra-pure water. This is due to the release of ionic species due to the degradation/modification of CA and not only of ZnO flowers. From a recent work based on analytical HPLC, it is known that CA might be subjected to deacetylation and weight loss in aqueous environments, demonstrating its biodegradability [66].

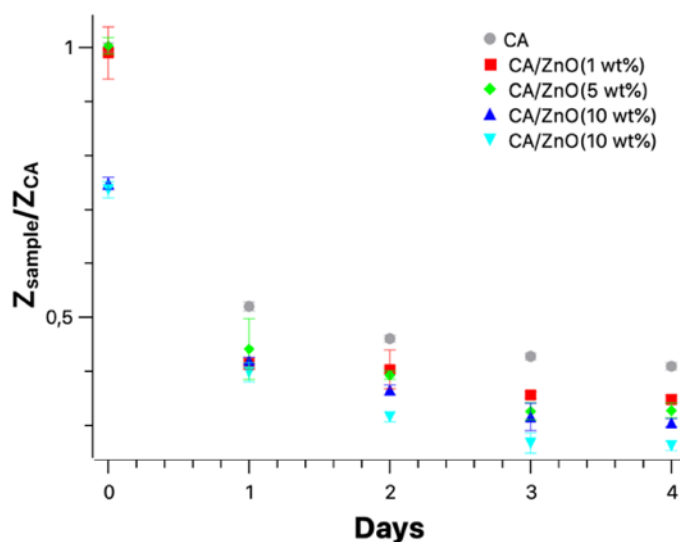


Figure 9. Monitoring ionic species release from the composites in ultra-pure water by EIS. The Z values measured at 5 kHz are normalized with respect to the CA samples measured the same day they were prepared. Each value is the average of three different measurements.

4. Conclusions

This work shows a new class of photocatalytic CA/ZnO composites combining rational synthesis of ZnO nanostructures and solution casting of biopolymeric films. The presence of ZnO flowers filler leads to a significant variation of the physical and chemical properties of the composite in a concentration dependent manner, increasing the thermal stability and modifying the surface

wettability, as a result of surface-to-bulk dispersion. The morphological investigations highlight that ZnO flowers tend to accumulate at the bottom surface of the composite and that at the highest loading 15 wt%, the formation of large clusters which lead to a significantly lower wettability in comparison to the 15 wt% loading.

The sample loaded with 10 wt% ZnO shows the best photocatalytic performances, in accordance with the higher hydrophobicity shown by the bottom face at the 15 wt% loading, along with the controlled release of zinc ions in solution triggered by simulated solar light. The stability of the composites is finally analyzed by EIS on the aqueous solution in which they are soaked, showing that both CA and ZnO contribute to the leakage of electrically conductive species in aqueous environments. These findings are a first step towards the exploitation of rational wet-chemistry based synthesis of ZnO structures usable as functional fillers in CA polymeric matrices for photocatalytic decontamination and controlled zinc ions release at nontoxic concentrations. Further studies will be directed towards the optimization of the ZnO structural features and dispersion strategies within the polymeric matrix to obtain light-responsive smart antifouling coatings.

CRedit authorship contribution statement

Giuseppe Arrabito: Conceptualization, Methodology, Resources, Data curation, Formal analysis, Investigation, Validation, Visualization, Funding acquisition, Writing – original draft, Writing – review & editing. **Giuseppe Prestopino:** Data curation, Formal analysis, Methodology, Investigation, Validation, Visualization, Project administration, Writing – original draft, Writing – review & editing. **Pier Gianni Medaglia:** Data curation, Formal analysis, Methodology, Investigation, Validation, Visualization. **Vittorio Ferrara:** Data curation, Formal analysis,

Methodology, Investigation, Validation, Visualization, Writing – original draft, Writing – review & editing. **Giuseppe Sancataldo:** Data curation, Formal analysis, Methodology, Investigation, Validation, Visualization. **Giuseppe Cavallaro:** Visualization, Data curation, Formal analysis, Investigation, Validation, Visualization, Writing – original draft, Writing – review & editing. **Francesco Di Franco:** Data curation, Formal analysis, Investigation, Validation, Visualization. **Michelangelo Scopelliti:** Data curation, Formal analysis, Methodology, Investigation, Validation, Visualization, Writing – original draft, Writing – review & editing. **Bruno Pignataro:** Supervision, Funding acquisition, Resources, Project administration, Writing – review & editing.

Declaration of Competing Interest

The authors declare that they have no known competing financial interests or personal relationships that could have appeared to influence the work reported in this paper.

Acknowledgements

This work has been funded by the European Union – NextGenerationEU – fondi MUR D.M. 737/2021 – research project “Zoomer”, CUP B79J21038330001. The Italian Ministry of University and Research (MURST, ex-MIUR) is acknowledged for funding through the PRIN 2022 project “2022WZK874 - Smart biopolymeric ZnO Nanowires composites for enhanced antibacterial activity”, CUP: B53D23015730006. This work has also been partially funded by European Union (NextGeneration EU), through the MUR-PNRR project SAMOTHRACE (ECS00000022). The Advanced Technologies Network (ATeN) Center (University of Palermo; project “Mediterranean Center for Human Health Advanced Biotechnologies (CHAB)”, PON R&C 2007-2013) is also acknowledged for hospitality and service.

Appendix A. Supplementary material

Supplementary materials. Additional optical characterization, Kubelka Munk plot for optical bandgap determination, Additional SEM characterizations, Multiplex fitting of the FTIR spectra, UV-VIS absorption spectra, Photocatalytic measurements, Impedance measurements, Zinc voltammetric sensor calibration.

Data availability

Data will be made available on request.

References

- [1] K. Sathya, K. Nagarajan, G. Carlin Geor Malar, S. Rajalakshmi, P. Raja Lakshmi, A comprehensive review on comparison among effluent treatment methods and modern methods of treatment of industrial wastewater effluent from different sources, *Appl. Water Sci.* 12 (2022) 70. <https://doi.org/10.1007/s13201-022-01594-7>.
- [2] A. Ashrafy, A.A. Liza, M.N. Islam, M.M. Billah, S.T. Arafat, M.M. Rahman, S.M. Rahman, Microplastics Pollution: A Brief Review of Its Source and Abundance in Different Aquatic Ecosystems, *J. Hazard. Mater. Adv.* 9 (2023) 100215. <https://doi.org/https://doi.org/10.1016/j.hazadv.2022.100215>.
- [3] M. Sharma, D. Rajput, V. Kumar, I. Jatain, T.M. Aminabhavi, G. Mohanakrishna, R. Kumar, K.K. Dubey, Photocatalytic degradation of four emerging antibiotic contaminants and toxicity assessment in wastewater: A comprehensive study, *Environ. Res.* 231 (2023) 116132. <https://doi.org/https://doi.org/10.1016/j.envres.2023.116132>.
- [4] H. Cheng, J. Wang, Y. Zhao, X. Han, Effect of phase composition {,} morphology {,} and

- specific surface area on the photocatalytic activity of TiO₂ nanomaterials, *RSC Adv.* 4 (2014) 47031–47038. <https://doi.org/10.1039/C4RA05509H>.
- [5] A.B.D. Nandiyanto, R. Zaen, R. Oktiani, Correlation between crystallite size and photocatalytic performance of micrometer-sized monoclinic WO₃ particles, *Arab. J. Chem.* 13 (2020) 1283–1296. <https://doi.org/10.1016/j.arabjc.2017.10.010>.
- [6] E. Fortunati, D. Puglia, I. Armentano, A. Valdés, M. Ramos, N. Juárez, M.C. Garrigós, J.M. Kenny, 8 - Multifunctional antimicrobial nanocomposites for food packaging applications, in: A.M.B.T.-F.P. Grumezescu (Ed.), *Nanotechnol. Agri-Food Ind.*, Academic Press, 2017: pp. 265–303. <https://doi.org/10.1016/B978-0-12-804303-5.00008-0>.
- [7] O. Eskikaya, S. Ozdemir, G. Tollu, N. Dizge, R. Ramaraj, A. Manivannan, D. Balakrishnan, Synthesis of two different zinc oxide nanoflowers and comparison of antioxidant and photocatalytic activity, *Chemosphere* 306 (2022) 135389. <https://doi.org/10.1016/j.chemosphere.2022.135389>.
- [8] A. Das, P. Mathan Kumar, M. Bhagavathiachari, R.G. Nair, Shape selective flower-like ZnO nanostructures prepared via structure-directing reagent free methods for efficient photocatalytic performance, *Mater. Sci. Eng. B Solid-State Mater. Adv. Technol.* 269 (2021) 115149. <https://doi.org/10.1016/j.mseb.2021.115149>.
- [9] V.J. Raj, R. Ghosh, A. Girigoswami, K. Girigoswami, Application of zinc oxide nanoflowers in environmental and biomedical science, *BBA Adv.* 2 (2022) 100051. <https://doi.org/10.1016/j.bbadv.2022.100051>.

- [10] S. Chatterjee, A.K. Kar, Synergistic influence of FRET, bulk recombination centers, and charge separation in enhancing the visible-light-driven photocatalytic activity of Cu²⁺-ion-doped ZnO nanoflowers, *Phys. Chem. Chem. Phys.* 24 (2022) 16281–16299. <https://doi.org/10.1039/D2CP01298G>.
- [11] M.K. Singha, A. Patra, V. Rojwal, K.G. Deepa, Single-step fabrication of ZnO microflower thin films for highly efficient and reusable photocatalytic activity, *J. Mater. Sci. Mater. Electron.* 31 (2020) 13578–13587. <https://doi.org/10.1007/s10854-020-03914-6>.
- [12] M. Pudukudy, Z. Yaakob, R. Rajendran, T. Kandaramath, Photodegradation of methylene blue over novel 3D ZnO microflowers with hexagonal pyramid-like petals, *React. Kinet. Mech. Catal.* 112 (2014) 527–542. <https://doi.org/10.1007/s11144-014-0703-5>.
- [13] A. Serrano-Lázaro, F.A. Verdín-Betancourt, V.K. Jayaraman, A. Hernández-Gordillo, M. de L. López-González, A. Sierra-Santoyo, G. Santana, M. Bizarro, Tracing the degradation pathway of temephos pesticide achieved with photocatalytic ZnO nanostructured films, *Environ. Sci. Nano* 9 (2022) 3538–3550. <https://doi.org/10.1039/D2EN00384H>.
- [14] A.H. Al Sharie, T. El-Elimat, R.S. Darweesh, S. Swedan, Z. Shubair, R. Al-Qiam, H. Albarqi, Green synthesis of zinc oxide nanoflowers using *Hypericum triquetrifolium* extract: characterization, antibacterial activity and cytotoxicity against lung cancer A549 cells, *Appl. Organomet. Chem.* 34 (2020) 1–13. <https://doi.org/10.1002/aoc.5667>.
- [15] A. Girigoswami, M. Ramalakshmi, N. Akhtar, S.K. Metkar, K. Girigoswami, ZnO

- Nanoflower petals mediated amyloid degradation - An in vitro electrokinetic potential approach, *Mater. Sci. Eng. C* 101 (2019) 169–178.
<https://doi.org/10.1016/j.msec.2019.03.086>.
- [16] J. Zhou, N.S. Xu, Z.L. Wang, Dissolving Behavior and Stability of ZnO Wires in Biofluids: A Study on Biodegradability and Biocompatibility of ZnO Nanostructures, *Adv. Mater.* 18 (2006) 2432–2435. <https://doi.org/10.1002/adma.200600200>.
- [17] P.P. Fu, Q. Xia, H.-M. Hwang, P.C. Ray, H. Yu, Mechanisms of nanotoxicity: Generation of reactive oxygen species, *J. Food Drug Anal.* 22 (2014) 64–75.
<https://doi.org/https://doi.org/10.1016/j.jfda.2014.01.005>.
- [18] S. Ostrovsky, G. Kazimirsky, A. Gedanken, C. Brodie, Selective cytotoxic effect of ZnO nanoparticles on glioma cells, *Nano Res.* 2 (2009) 882–890.
<https://doi.org/10.1007/s12274-009-9089-5>.
- [19] Y. Song, Z. Shi, G.-H. Hu, C. Xiong, A. Isogai, Q. Yang, Recent advances in cellulose-based piezoelectric and triboelectric nanogenerators for energy harvesting: a review, *J. Mater. Chem. A* 9 (2021) 1910–1937. <https://doi.org/10.1039/D0TA08642H>.
- [20] W. Deng, T. Yang, L. Jin, C. Yan, H. Huang, X. Chu, Z. Wang, D. Xiong, G. Tian, Y. Gao, H. Zhang, W. Yang, Cowpea-structured PVDF/ZnO nanofibers based flexible self-powered piezoelectric bending motion sensor towards remote control of gestures, *Nano Energy* 55 (2019) 516–525. <https://doi.org/10.1016/j.nanoen.2018.10.049>.
- [21] N.B. Erdal, M. Hakkarainen, Degradation of Cellulose Derivatives in Laboratory, Man-Made, and Natural Environments, *Biomacromolecules* 23 (2022) 2713–2729.

- <https://doi.org/10.1021/acs.biomac.2c00336>.
- [22] H. Seddiqi, E. Oliaei, H. Honarkar, J. Jin, L.C. Geonzon, R.G. Bacabac, J. Klein-Nulend, Cellulose and its derivatives: towards biomedical applications, Springer Netherlands, 2021. <https://doi.org/10.1007/s10570-020-03674-w>.
- [23] K. Zhang, C. Mo, X. Tang, X. Lei, Hierarchically Porous Cellulose-Based Radiative Cooler for Zero-Energy Food Preservation, ACS Sustain. Chem. Eng. (2023). <https://doi.org/10.1021/acssuschemeng.3c00170>.
- [24] C. Chiappara, G. Arrabito, V. Ferrara, M. Scopelliti, G. Sancataldo, V. Vetri, D.F. Chillura Martino, B. Pignataro, Improved Photocatalytic Activity of Polysiloxane TiO₂Composites by Thermally Induced Nanoparticle Bulk Clustering and Dye Adsorption, Langmuir 37 (2021) 10354–10365. <https://doi.org/10.1021/acs.langmuir.1c01475>.
- [25] S. Fabiano, B. Pignataro, Selecting speed-dependent pathways for a programmable nanoscale texture by wet interfaces, Chem. Soc. Rev. 41 (2012) 6859–6873. <https://doi.org/10.1039/C2CS35074B>.
- [26] H. Patnam, S.A. Graham, J.S. Yu, Y-ZnO Microflowers Embedded Polymeric Composite Films to Enhance the Electrical Performance of Piezo/Tribo Hybrid Nanogenerators for Biomechanical Energy Harvesting and Sensing Applications, ACS Sustain. Chem. Eng. 9 (2021) 4600–4610. <https://doi.org/10.1021/acssuschemeng.1c00025>.
- [27] N. Čelić, N. Banić, I. Jagodić, R. Yatskiv, J. Vaniš, G. Štrbac, S. Lukić-Petrović, Eco-Friendly Photoactive Foils Based on ZnO/SnO₂-PMMA Nanocomposites with High

- Reuse Potential, *ACS Appl. Polym. Mater.* (2023).
<https://doi.org/10.1021/acsapm.3c00396>.
- [28] Y. Peng, H. Zhou, Y. Wu, Z. Ma, L. Tian, L. Jiang, Facile synthesis of Flower-like ZnO loading Cellulose-Chitosan nanocomposite films by biomimetic approach with enhanced performance, *Appl. Surf. Sci.* 614 (2023) 156119.
<https://doi.org/10.1016/j.apsusc.2022.156119>.
- [29] E.D. Mohamed Isa, N.W. Che Jusoh, R. Hazan, K. Shameli, Photocatalytic degradation of methyl orange using pullulan-mediated porous zinc oxide microflowers, *Environ. Sci. Pollut. Res.* 28 (2021) 5774–5785. <https://doi.org/10.1007/s11356-020-10939-1>.
- [30] G. Arrabito, V. Errico, Z. Zhang, W. Han, C. Falconi, Nanotransducers on printed circuit boards by rational design of high-density, long, thin and untapered ZnO nanowires, *Nano Energy* 46 (2018) 54–62. <https://doi.org/10.1016/j.nanoen.2018.01.029>.
- [31] R. López, R. Gómez, Band-gap energy estimation from diffuse reflectance measurements on sol-gel and commercial TiO₂: A comparative study, *J. Sol-Gel Sci. Technol.* 61 (2012) 1–7. <https://doi.org/10.1007/s10971-011-2582-9>.
- [32] S.M. da Silva, A.L. Squizzato, D.P. Rocha, M.L.S. Vasconcellos, R. de Q. Ferreira, E.M. Richter, R.A.A. Munoz, Improved anodic stripping voltammetric detection of zinc on a disposable screen-printed gold electrode, *Ionics (Kiel)*. 26 (2020) 2611–2621.
<https://doi.org/10.1007/s11581-019-03379-6>.
- [33] J. Ma, J. Ren, Y. Jia, Z. Wu, L. Chen, N.O. Haugen, H. Huang, Y. Liu, High efficiency bi-harvesting light/vibration energy using piezoelectric zinc oxide nanorods for dye

- decomposition, *Nano Energy* 62 (2019) 376–383.
<https://doi.org/10.1016/j.nanoen.2019.05.058>.
- [34] J. Liu, J. Cao, Z. Li, G. Ji, M. Zheng, A simple microwave-assisted decomposing route for synthesis of ZnO nanorods in the presence of PEG400, *Mater. Lett.* 61 (2007) 4409–4411.
<https://doi.org/https://doi.org/10.1016/j.matlet.2007.02.014>.
- [35] D. Liu, Y. Lv, M. Zhang, Y. Liu, Y. Zhu, R. Zong, Y. Zhu, Defect-related photoluminescence and photocatalytic properties of porous ZnO nanosheets, *J. Mater. Chem. A* 2 (2014) 15377–15388. <https://doi.org/10.1039/C4TA02678K>.
- [36] A. McLaren, T. Valdes-Solis, G. Li, S.C. Tsang, Shape and size effects of ZnO nanocrystals on photocatalytic activity, *J. Am. Chem. Soc.* 131 (2009) 12540–12541.
<https://doi.org/10.1021/ja9052703>.
- [37] K.K. Taha, M. Al Zoman, M. Al Outeibi, S. Alhussain, A. Modwi, A.A. Bagabas, Green and sonogreen synthesis of zinc oxide nanoparticles for the photocatalytic degradation of methylene blue in water, *Nanotechnol. Environ. Eng.* 4 (2019) 1–11.
<https://doi.org/10.1007/s41204-019-0057-3>.
- [38] O. Yayapao, T. Thongtem, A. Phuruangrat, S. Thongtem, Sonochemical synthesis of Dy-doped ZnO nanostructures and their photocatalytic properties, *J. Alloys Compd.* 576 (2013) 72–79. <https://doi.org/https://doi.org/10.1016/j.jallcom.2013.04.133>.
- [39] G. Xiong, U. Pal, J.G. Serrano, Correlations among size, defects, and photoluminescence in ZnO nanoparticles, *J. Appl. Phys.* 101 (2007) 24317.
<https://doi.org/10.1063/1.2424538>.

- [40] S. Marković, I. Stojković Simatović, S. Ahmetović, L. Veselinović, S. Stojadinović, V. Rac, S.D. Škapin, D. Bajuk Bogdanović, I. Janković Častvan, D. Uskoković, Surfactant-assisted microwave processing of ZnO particles: A simple way for designing the surface-to-bulk defect ratio and improving photo(electro)catalytic properties, *RSC Adv.* 9 (2019) 17165–17178. <https://doi.org/10.1039/c9ra02553g>.
- [41] S. Wongsasulak, M. Patapeejumruswong, J. Weiss, P. Supaphol, T. Yoovidhya, Electrospinning of food-grade nanofibers from cellulose acetate and egg albumen blends, *J. Food Eng.* 98 (2010) 370–376. <https://doi.org/https://doi.org/10.1016/j.jfoodeng.2010.01.014>.
- [42] T. Sudiarti, D. Wahyuningrum, B. Bundjali, I. Made Arcana, Mechanical strength and ionic conductivity of polymer electrolyte membranes prepared from cellulose acetate-lithium perchlorate, *IOP Conf. Ser. Mater. Sci. Eng.* 223 (2017). <https://doi.org/10.1088/1757-899X/223/1/012052>.
- [43] A.S. Figueiredo, A.R. Garcia, M. Minhalma, L. Ilharco, M.N. De Pinho, The ultrafiltration performance of cellulose acetate asymmetric membranes: A new perspective on the correlation with the infrared spectra, *J. Membr. Sci. Res.* 6 (2020) 70–80. <https://doi.org/10.22079/JMSR.2019.110424.1269>.
- [44] A. Kramar, I. Rodríguez Ortega, G. González-Gaitano, J. González-Benito, Solution casting of cellulose acetate films: influence of surface substrate and humidity on wettability, morphology and optical properties, *Cellulose* 30 (2023) 2037–2052. <https://doi.org/10.1007/s10570-022-05026-2>.

- [45] M. Diantoro, A.A. Mustikasari, N. Wijayanti, C. Yogihati, A. Taufiq, Microstructure and dielectric properties of cellulose acetate-ZnO/ITO composite films based on water hyacinth, *J. Phys. Conf. Ser.* 853 (2017). <https://doi.org/10.1088/1742-6596/853/1/012047>.
- [46] I. Pérez-Silva, M.E. Páez-Hernández, I.S. Ibarra, R.L. Camacho-Mendoza, Evaluation of the Hybrid Membrane of ZnO Particles Supported in Cellulose Acetate for the Removal of Lead, *Membranes (Basel)*. 13 (2023). <https://doi.org/10.3390/membranes13020123>.
- [47] S. Anitha, B. Brabu, D.J. Thiruvadigal, C. Gopalakrishnan, T.S. Natarajan, Optical, bactericidal and water repellent properties of electrospun nano-composite membranes of cellulose acetate and ZnO, *Carbohydr. Polym.* 87 (2012) 1065–1072. <https://doi.org/https://doi.org/10.1016/j.carbpol.2011.08.030>.
- [48] H. Helmiyati, Z.S.Z. Hidayat, I.F.R. Sitanggang, D. Liftyawati, Antimicrobial packaging of ZnO–Nps infused into CMC–PVA nanocomposite films effectively enhances the physicochemical properties, *Polym. Test.* 104 (2021) 107412. <https://doi.org/https://doi.org/10.1016/j.polymertesting.2021.107412>.
- [49] A.M. Asiri, V. Pugliese, F. Petrosino, S.B. Khan, K.A. Alamry, S.Y. Alfifi, H.M. Marwani, M.M. Alotaibi, D. Mukherjee, S. Chakraborty, Photocatalytic Degradation of Textile Dye on Blended Cellulose Acetate Membranes, *Polymers* 14 (2022). <https://doi.org/10.3390/polym14030636>.
- [50] M. Onyszko, A. Markowska-Szczupak, R. Rakoczy, O. Paszkiewicz, J. Janusz, A. Gorgon-Kuza, K. Wenelska, E. Mijowska, The cellulose fibers functionalized with star-

- like zinc oxide nanoparticles with boosted antibacterial performance for hygienic products, *Sci. Rep.* 12 (2022) 1–13. <https://doi.org/10.1038/s41598-022-05458-7>.
- [51] H. Orelma, A. Hokkanen, I. Leppänen, K. Kammiovirta, M. Kapulainen, A. Harlin, Optical cellulose fiber made from regenerated cellulose and cellulose acetate for water sensor applications, *Cellulose* 27 (2020) 1543–1553. <https://doi.org/10.1007/s10570-019-02882-3>.
- [52] R. Al-Gaashani, S. Radiman, A.R. Daud, N. Tabet, Y. Al-Douri, XPS and optical studies of different morphologies of ZnO nanostructures prepared by microwave methods, *Ceram. Int.* 39 (2013) 2283–2292. <https://doi.org/10.1016/j.ceramint.2012.08.075>.
- [53] G. Cavallaro, G. Lazzara, S. Milioto, Nanocomposites based on halloysite nanotubes and sulphated galactan from red seaweed *Gloiopeltis*: Properties and delivery capacity of sodium diclofenac, *Int. J. Biol. Macromol.* 234 (2023) 123645. <https://doi.org/10.1016/j.ijbiomac.2023.123645>.
- [54] I. Kovinchuk, N. Haiuk, G. Lazzara, G. Cavallaro, G. Sokolsky, Enhanced photocatalytic degradation of PE film by anatase/ γ -MnO₂, *Polym. Degrad. Stab.* 210 (2023) 110295. <https://doi.org/10.1016/j.polymdegradstab.2023.110295>.
- [55] R. Mardosaitė, A. Jurkevičiūtė, S. Račkauskas, Superhydrophobic ZnO Nanowires: Wettability Mechanisms and Functional Applications, *Cryst. Growth Des.* 21 (2021) 4765–4779. <https://doi.org/10.1021/acs.cgd.1c00449>.
- [56] L. Lisuzzo, G. Cavallaro, S. Milioto, G. Lazzara, Halloysite nanotubes as nanoreactors for heterogeneous micellar catalysis, *J. Colloid Interface Sci.* 608 (2022) 424–434.

- <https://doi.org/10.1016/j.jcis.2021.09.146>.
- [57] M. Zhang, Y. Jia, M. Gao, L. Ren, B.Z. Tang, Photo-triggered Zn²⁺ release for the regulation of zinc enzymes, *Mater. Chem. Front.* 5 (2021) 1824–1829.
<https://doi.org/10.1039/D0QM00947D>.
- [58] J. Han, W. Qiu, W. Gao, Potential dissolution and photo-dissolution of ZnO thin films, *J. Hazard. Mater.* 178 (2010) 115–122. <https://doi.org/10.1016/j.jhazmat.2010.01.050>.
- [59] D. Cardoso, A. Narcy, S. Durosoy, C. Bordes, Y. Chevalier, Dissolution kinetics of zinc oxide and its relationship with physicochemical characteristics, *Powder Technol.* 378 (2021) 746–759. <https://doi.org/10.1016/j.powtec.2020.10.049>.
- [60] J. Pasquet, Y. Chevalier, J. Pelletier, E. Couval, D. Bouvier, M.A. Bolzinger, The contribution of zinc ions to the antimicrobial activity of zinc oxide, *Colloids Surfaces A Physicochem. Eng. Asp.* 457 (2014) 263–274.
<https://doi.org/10.1016/j.colsurfa.2014.05.057>.
- [61] P. Sitarik, D.C. Martin, Salt Solution Concentration Effects on the Electrochemical Impedance Spectroscopy of Poly(3,4-ethylenedioxythiophene) (PEDOT), *ChemElectroChem* 9 (2022). <https://doi.org/10.1002/celec.202200231>.
- [62] T. Addabbo, A. Fort, M. Mugnaini, L. Parri, M. Pinzi, V. Vignoli, P.K. Mvemba, M. Becatti, V. Barygina, N. Taddei, C. Fiorillo, On the Suitability of Low-Cost Compact Instrumentation for Blood Impedance Measurements, *IEEE Trans. Instrum. Meas.* 68 (2019) 2412–2424. <https://doi.org/10.1109/TIM.2019.2899475>.

- [63] T. Addabbo, A. Fort, P. Kapita, M. Mugnaini, V. Vignoli, V. Barygina, M. Becatti, C. Fiorillo, N. Taddei, A Compact System for Blood Impedance Measurements for ROS Evaluation, *MeMeA 2018 - 2018 IEEE Int. Symp. Med. Meas. Appl. Proc.* (2018). <https://doi.org/10.1109/MeMeA.2018.8438784>.
- [64] A. Zhu, Y. Liu, Q. Rui, Y. Tian, Selective and sensitive determination of hydroxyl radicals generated from living cells through an electrochemical impedance method, *Chem. Commun.* 47 (2011) 4279–4281. <https://doi.org/10.1039/c0cc05821a>.
- [65] A. Sadkowski, J.P. Diard, On the Fletcher's two-terminal equivalent network of a three-terminal electrochemical cell, *Electrochim. Acta* 55 (2010) 1907–1911. <https://doi.org/10.1016/j.electacta.2009.11.008>.
- [66] N. Yadav, M. Hakkarainen, Degradation of Cellulose Acetate in Simulated Aqueous Environments: One-Year Study, *Macromol. Mater. Eng.* 307 (2022) 1–9. <https://doi.org/10.1002/mame.202100951>.